Research Square

Preprints are preliminary reports that have not undergone peer review.
They should not be considered conclusive, used to inform clinical practice,
or referenced by the media as validated information.

Graphene-Engineered NiFe-LDH Nanocomposites with Surface- Controlled Charge Storage for High-Performance Supercapacitors

Ruhi Siddiqui
Dr. A.P.J. Abdul Kalam Technical University
Moin Ali Siddiqui
Indian Institute of Technology Jodhpur
A V Ullas
Dr. A.P.J. Abdul Kalam Technical University
Manjunatha C
RV College of Engineering
Prashant Kumar Gupta
Indian Institute of Technology Jodhpur
Chandresh Kumar Rastogi
chandreshkumar.rastogi@rait.ac.in

Ramrao Adik Institute of Technology

Research Article

Keywords: Layered double hydroxide (LDH), NiFe-LDH, Graphene, Pseudo capacitance, Electrochemical kinetics, Supercapacitor, Charge storage mechanism

Posted Date: October 23rd, 2026

DOI: https://doi.org/10.21203/rs.3.rs-10988233/v1

License: This work is licensed under a Creative Commons Attribution 4.0 International License.
Read Full License

Additional Declarations: No competing interests reported.

Graphene-Engineered NiFe-LDH Nanocomposites with Surface-Controlled Charge Storage for High-Performance Supercapacitors

Ruhi Siddiqui[1], Moin Ali Siddiqui[2], A.V. Ullas[1], C. Manjunatha[3], Prashant Kumar Gupta[4,], Chandresh Kumar Rastogi[1,5*]*

[1]Nanotechnology Program, Centre for Advanced Studies, AKTU, Lucknow (226031), India.

[2]Department of Materials Engineering, Indian Institute of Technology Jodhpur, Rajasthan (342030), India.

[3]Department of Chemistry, RV College of Engineering, Bengaluru-560059, India

[4]Department of Chemical Engineering, Indian Institute of Technology Jodhpur, Rajasthan (342030), India.

[5]Department of Engineering Science, Ramrao Adik Institute of Technology, Dr. D. Y. Patil Vidyapeeth, Navi Mumbai, Maharashtra (400706), India.

Corresponding Authors' Emails: chandreshkumar.rastogi@rait.ac.in and guptapk@iitj.ac.in

Abstract

Nickel-iron layered double hydroxide (NiFe-LDH) is a promising pseudo-capacitive electrode material; however, its electrochemical performance is limited by poor electrical conductivity and the tendency of LDH nanosheets to form agglomerates. Herein, to overcome both challenges, we have employed a one-pot hydrothermal method to synthesize a NiFe-LDH-Graphene nanocomposite (NiFe-LDH@Graphene), in which the two-dimensional graphene interface provides conductive electron transport pathways while inhibiting the formation of aggregates. BET Analysis revealed a 17% enhancement in surface area (S_{BET}) after inclusion with graphene, with values being ~41.4 and 48.5 %, for bare NiFe-LDH and NiFe-LDH@Graphene, respectively. The electrode fabricated from NiFe-LDH@Graphene nanostructure showcases an enhanced specific capacitance up to 953 F g^{-1} at 1 A g^{-1} (representing a 138% increase in C_s, vis-à-vis ~400 F g^{-1} for bare NiFe-LDH) with an energy density of 26.81 Wh kg^{-1} at a power density of 224.89 W kg^{-1}, respectively. Power-law analysis carried out using cyclic voltammograms at varying scanning rates clearly demonstrated a change in the charge storage behavior from nearly diffusion-controlled (b = 0.419) for pure NiFe-LDH to surface-controlled for NiFe-LDH@Graphene (b = 0.868). These findings clearly indicate improved contribution of faradic and capacitive processes at the surface due to the

integration of graphene sheets into NiFe-LDH. Furthermore, NiFe-LDH@Graphene electrode retains a higher capacitance retention (CR) of ~90.2% after 6000 Galvanostatic charge-discharge (GCD) cycles, outperforming pristine NiFe-LDH by 17%, with a CR value of ~ 73.2%. This improvement is attributed to the conducting 2D graphene structure, which suppresses nanosheet restacking while facilitating electron transport. Collectively, these results position planar carbon scaffolding as an electronically and geometrically superior engineering strategy for high-performance pseudocapacitive electrodes.

Keywords: Layered double hydroxide (LDH); NiFe-LDH; Graphene; Pseudo capacitance; Electrochemical kinetics; Supercapacitor; Charge storage mechanism

1. Introduction

The growing concerns associated with climate change, the depletion of fossil fuel reserves, and the ever-increasing global energy demand have created an urgent need to develop renewable energy systems and advanced energy storage (EES) technologies [1,2]. Supercapacitors (SC_s), formally known as electrochemical capacitive energy storage, bridge the performance gap between conventional dielectric capacitors and rechargeable batteries [3]. They gained significant attention for their instantaneous power-delivery capability, rapid charge-discharge kinetics, durable cycling performance, and safety [4,5]. Supercapacitors are categorized into electric double-layer capacitors (EDLCs) and Pseudocapacitors. EDLCs store charge electrostatically through non-Faradaic ion adsorption at the electrode-electrolyte interface. [6,7] Pseudocapacitors exploit fast reversible Faradaic reactions for higher capacitance and energy density, and hybrid supercapacitors, which integrate both mechanisms in a single device [8-10]. Despite their high-power density, rapid charge-discharge capability, and exceptional cycling stability, the widespread application of supercapacitors is still constrained by their low energy density and the poor electrical conductivity, sluggish charge-transfer kinetics, and limited electrochemical utilization of many pseudocapacitive electrode materials. Therefore, rational engineering of electrode materials is essential for achieving superior supercapacitor performance [11-13]. The performance of a supercapacitor depends on the composition, morphology, porosity, crystal structure, and redox activity of the electrode material [11].

In past, researchers have extensively investigated a wide range of transition metal oxide based electrode material (e.g. Co_3O_4, NiO, ZnO, Fe_2O_3, RuO_2, $NiCo_2O_4$, $CuCoO_2$, and $MnFe_2O_4$) [7,8,9,13], hydroxides (e.g., $Ni(OH)_2$, $Co(OH)_2$, and NiFe-LDH) [12], sulfides (e.g., NiS,

$NiCo_2S_4$, and MoS_2) [15], selenides (e.g., $NiSe_2$, $CoSe_2$, and $MoSe_2$), phosphides (e.g., Ni_2P, CoP, and FeP) [13-16]. In particular, layered double hydroxides (LDHs) have secured a prominent position among Faradaic SC electrode candidates by virtue of an intrinsically advantageous crystal architecture. The LDHs structure consists of positively charged, brucite-derived metal hydroxide sheets built from edge-sharing $M(OH)_6$ octahedra in which a portion of the divalent M(II) sites are occupied by trivalent M(III) cations whose net layer charge is neutralized by hydrated, exchangeable anions lodged in the interlayer space, yielding the compositional formula $[M^{2+}_{1-x}M^{3+}_x(OH)_2]^{x+}[A^{n-}_{x/n}] \cdot mH_2O$. Three structural features make this class of material particularly attractive for SC electrodes. The uniformly distributed multivalent metal centres supply a high areal density of Faradaic active sites accessible to the electrolyte [16-18]. The expandable interlayer galleries allow reversible OH^- intercalation and de-intercalation in alkaline media, shortening the effective ionic diffusion length. Due to the flexibility in the chemical composition, M(II) can be chosen among Ni^{2+}, Co^{2+}, Fe^{2+}, and $Mn^{2+,}$ while M(III) can be chosen among Al^{3+}, Fe^{3+}, and Cr^{3+} ions. These ions facilitate fine-tuning of the redox potential range and electronic structure [19].

Among the various LDH compositions, NiFe-LDH is considered one of the most promising pseudocapacitive electrode materials due to its rich redox activity, favorable electronic conductivity, high theoretical capacitance, synergistic interaction between Fe and Ni cations, and cost-effective preparation. [20,21]. Two different types of cations, Ni^{2+}/Ni^{3+} and Fe^{2+}/Fe^{3+} participate separately in charge storage via redox reactions involving OH^- ions. The Fe^{3+} ions present in the hydroxide layer affect the electronic environment of the neighboring Ni^{2+} cations, lowering the activation energy of the oxidation process $Ni^{2+} \rightarrow Ni^{3+}$ and increasing the redox potential window [20]. Though a bare NiFe-LDH-based electrode showcases prominent electrochemical properties, these are constrained by a few structurally interconnected barriers that ultimately hinder it from achieving its full potential in practical applications. They exhibit extremely low intrinsic electrical conductivity, leading to high charge-transfer resistance between redox-active sites and the current collector, resulting in significant ohmic losses at any current density [21,22]. Furthermore, the LDH nanosheets underwent agglomeration due to face-to-face alignment, driven by van der Waals and interlayer hydrogen bonds, eventually leading to the collapse of the interlayer galleries during electrode formation, leaving behind electrochemically inaccessible Ni and Fe redox centers. Thethe particle aggregation aggravates the ion migration resistance caused by the poor electrical conductivity of NiFe-LDHs. As a result, the charge-discharge process occurs more rapidly than the diffusion of OH^- ions through

the highly resistive electrode matrix [23-25]. Besides structural degradation, bare NiFe-LDH suffers from the dissolution of lattice metal ions and the Jahn-Teller distortion of Ni^{3+}, leading to irreversible structural deformation, loss of electrochemically active sites, increased charge-transfer resistance, and rapid capacitance fading during prolonged cycling [24].

Integration of NiFe-LDH nanosheets into a conductive scaffold represents an effective engineering strategy that serves both as an electron-transport highway and as a physical spacer to prevent nanosheet restacking. Zhou et al. [26] anchored NiFe-LDH onto Ti_3C_2 MXene, which resulted in 720.2 F g^{-1} at 1 A g^{-1} with 84% retention at 1000 cycles. However, the HF-dependent etching and multi-step processing make this route commercially impractical. Rabbani et al. [27] synthesized $NiCo_2S_4$@NiFe-LDH heterostructures employing a three-step hydrothermal method, which delivered 827 F g^{-1} with 90.2% retention after 12,000 cycles. The incorporation of CNTs into NiFe-LDH has been proven to improve the stability and charge storage capacity. For instance, Chavan et al. [12] reported that LDH@ CNT electrode showed an improved specific capacitance (C_s) of 1243 F g^{-1} and capacitance retention (CR) of 87% after 6000 cycles (N) compared to the bare NiFe-LDH electrode (C_s = 834 F g^{-1}; CR ~ 73% and N = 6000). Zhou et al. [26] reported NiFe-LDH/MXene composite electrode retained 86% after 1000 cycles, compared to only 24% for bare NiFe-LDH. Wang et al. [16] obtained 97.1% after 2500 cycles using NiFe-LDH/RGO/CNFs. However, both rely on complicated multi-stage synthetic protocols, making scalability difficult. Importantly, despite the range of studies conducted in this regard, little is known about the role of graphene in determining the structural stability and capacitance retention behavior of NiFe-LDH specifically.

Recently, graphene has emerged as the most geometrically and electronically compatible support architecture for LDH-based materials. It is comprised of a two-dimensional (2D), atomically thin basal plane with extraordinary in-plane electrical conductivity, a theoretical specific surface area of 2630 m^2g^{-1}, and a surface chemistry amenable to functionalization, which collectively promote dense, uniform nucleation of LDH nanosheets across the basal plane and establish a dimensionally matched, face-to-face LDH-graphene heterointerface with maximized electroactive contact area [24,25]. In systems analogous to NiFe-LDH like NiAl/CoAl-LDHs, graphene has also been shown to be effective as a 2D LDH support for enhanced electrochemical characteristics. For instance, Gao et al. [25] employed a hydrothermal method to homogeneously grow NiAl-LDH over graphene nanosheets (GNS) to produce NiAl-LDH@GNS with a specific capacitance of 781.5 F g^{-1}. A specific capacitance

value of 838 F g^{-1} with a 95% retention rate was obtained after 20,000 Faradaic cycles in the case of Co-Al-LDH through organic intercalation by Zai et al. [28].

Despite extensive research on hybrid NiFe-LDH-based materials, the mechanistic contribution of graphene toward enhancing charge-storage kinetics and electrochemical characteristics of NiFe-LDH has yet to be fully elucidated. The present study addresses this gap by investigating the role of graphene in enhancing the electrochemical durability of LDH-based supercapacitor electrodes. In this direction, a facile, scalable, quick, and cost-effective technique, the single-step hydrothermal method, has been devised to design NiFe-LDH@Graphene architectures, and in-depth physical and electrochemical characterizations have been carried out regarding supercapacitor applications. The nanocomposites showed a 2.4 times higher capacitance, enhanced from 400 F g^{-1} for bare NiFe LDH to 953 F g^{-1} for the NiFe LDH@Graphene nanocomposite at 1 A g^{-1}. Furthermore, the graphene had an energy density of 26.81 Wh kg^{-1}, given at 224.89 W kg^{-1}. Bare NiFe-LDH exhibits predominantly diffusion-controlled charge storage, whereas the NiFe-LDH@graphene hybrid displays predominantly surface-controlled (capacitive) charge storage. Furthermore, the graphene-integrated NiFe LDH showcases an exceptional enhancement in capacitance retention up to 90.2% after 6,000 galvanostatic charge-discharge (GCD) cycles as compared to 73.2 % for bare NiFe LDH under the same measurement conditions. In brief, the conductive and flexible graphene network facilitates rapid charge transport, prevents LDH aggregation, and alleviates structural deterioration during prolonged electrochemical cycling. This underscores the crucial role of the 2D carbon framework in preserving electrode integrity and ensuring long-term cycling stability.

2. Experimental section

2.1 Materials

All synthetic precursor reagents were commercially procured from Sigma-Aldrich, and used as such without any other treatment: nickel(II) nitrate hexahydrate ($Ni(NO_3)_2 \cdot 6H_2O$, purity ≥99%), iron(II) sulfate heptahydrate ($FeSO_4 \cdot 7H_2O$, purity ≥99%), urea ($CO(NH_2)_2$, purity ≥99%), sodium acetate (CH_3COONa, purity ≥99%), and graphene nanoplatelets possessing a platelet thickness of 5-10 nm and lateral size of ~5 μm. PVDF and NMP, purchased from Sigma-Aldrich, were used as a polymer binder and solvent, respectively, for preparing electrode slurries. A 6 M aqueous electrolyte solution was freshly prepared by dissolution of pellets of potassium hydroxide (KOH, purity ≥99%, Merck) in deionized water with continuous

stirring. The purity level of all chemical reagents used in experiments was of the analytical grade, and these reagents were used without any further purification process.

2.2 Synthesis of NiFe-LDH and Graphene Nanoplatelet Composites

Pristine NiFe-LDH was synthesized via single-step hydrothermal coprecipitation. Initially, 60 mL of an aqueous solution of 1861.2 mg $Ni(NO_3)_2 \cdot 6H_2O$ (6.4 mmol), 444.8 mg $FeSO_4 \cdot 7H_2O$ (1.6 mmol), 864.8 mg urea (14.4 mmol), and 6.58 mg sodium acetate (0.08 mmol) was prepared by continuous stirring at room temperature for 4 h. The solution was transferred to a 100 mL Teflon-lined stainless-steel autoclave and placed in a preheated hot air oven at 150 °C for 6 h. Thereafter, the reaction mixture was allowed to cool naturally to yield a green yellowish colour precipitate. The as-obtained precipitate was washed thrice with deionized water and acetone and dried at 80 °C for 4 h under vacuum to yield NiFe-LDH nanomaterial.

Similarly, NiFe-LDH@Graphene nanocomposite was prepared using the same protocol, except the addition of 60 mL aqueous solution of 10 mg graphene into the reaction mixture under continuous stirring conditions for 4 h before placing in the reactor for heat treatment. **Figure 1.** illustrates the protocol used for the synthesis of Ni-Fe LDH nanomaterials.

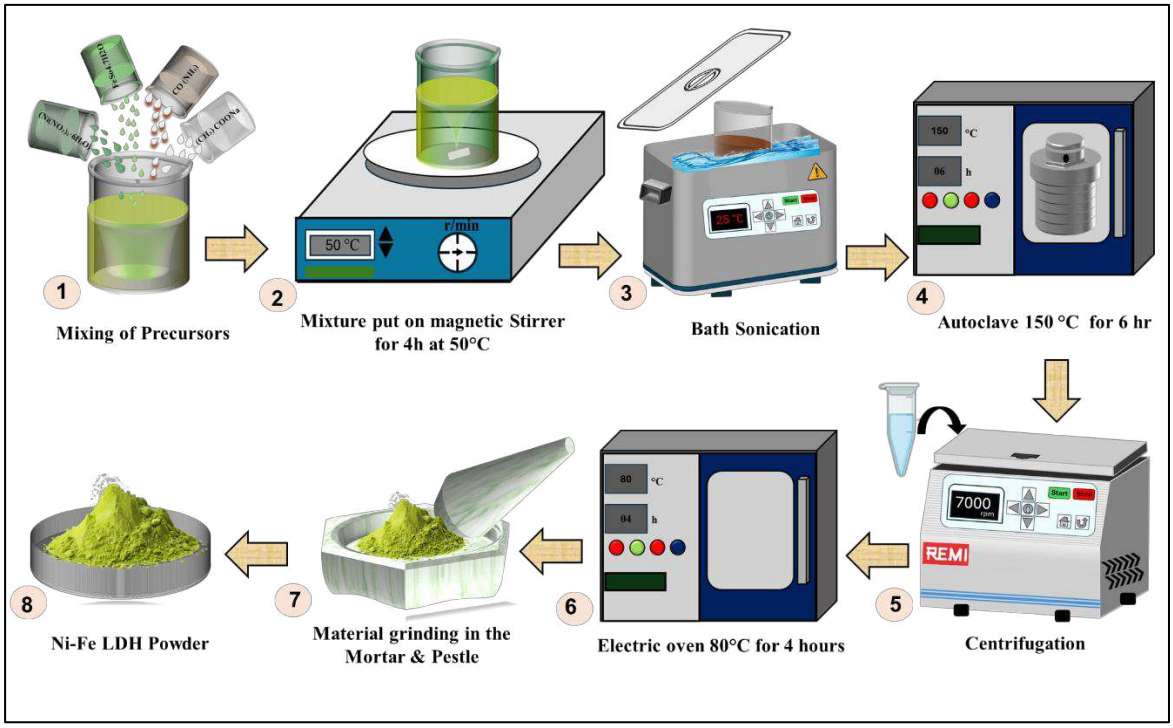


Figure 1. Schematic depicting the protocol used for the hydrothermal synthesis of NiFe-LDH nanomaterials.

2.3 Materials Characterization

Crystallographic phase analysis was performed using the X-ray diffractometer model PANalytical X'Pert PRO, where samples were exposed to radiation from Cu Kα (λ = 1.5406 Å), with reflections measured at intervals of 0.02° while scanning between angles of 2θ = 10 to 90° at a constant speed of 2° min^{-1}. Average crystalline grain sizes were later calculated using the most prominent (003) diffraction peak using the mathematics developed by the Debye-Scherrer formula. Surface morphologies and nanostructure were assessed using a Zeiss Sigma 300 field emission scanning electron microscope operated at a beam energy of 10 keV, while elemental analysis, along with two-dimensional compositional distributions, was concurrently performed using an Oxford Instruments X-Max 80 energy dispersive spectrometer. Molecular vibrations and chemical bonding states were investigated using vibrational spectroscopy on a Thermo Fisher Nicolet Summit X machine operated under attenuated total reflection geometry over a range of wavenumbers between 400 and 4000 cm^{-1}, operating continuously at an instrumental resolution of 4 cm^{-1}. Atomic imaging and interfacial crystal lattice structures were visualized via high-resolution transmission electron microscopy on a Thermo Fisher Talos F200i device operated at 200 keV beam energy. Specific surface area analysis and porosity were achieved via gas absorption measurements using nitrogen under low-temperature conditions, utilizing a Micromeritics ASAP 2020 volumetric analysis system, while all BET calculations were constrained to adsorption data within the pressure ratio region of $0.05 \leq P/P_o \leq 0.30$. The electrochemical investigation processes were performed consistently under thermal stabilization within an electrochemical cell operating at 25 ± 2 °C using a Metrohm Autolab PGSTAT302N potentiostat as the main electroanalytical equipment. The electrochemical testing was performed in a three-compartment setup, where the working electrode was represented by the active substance applied to carbon paper, charge balance maintenance was ensured by a platinum mesh of size 1 × 2 cm^2 used as an auxiliary electrode, while reference was provided with the help of a mercury-mercury oxide (Hg/HgO) oxide half-cell filled with a 1 M potassium hydroxide solution. The electrolyte consisted of an aqueous 6 M potassium hydroxide solution. All electrodes were conditioned with respect to their open circuit potential before the experiments for 30 min. Electrochemical characterization was conducted in the range of voltages between -0.4 and +0.4 V with a scan rates in the range 10-100 mV/s. Galvanostatic charge-discharge characteristics were recorded at current densities in the range 1-5 A g^{-1}. Capacitance values based on gravimetric data were determined mathematically by discharging transient curves using the formula $C_s = (I \times \Delta t)/(m \times \Delta V)$, where

I stands for discharge current value (A), Δt is the total duration of discharging period (s), m is the amount of deposited active material (g), and ΔV represents net operational voltage excluding any effects due to resistance (V). For assessing the durability of operation cycles, galvanostatic cycling was conducted continuously at a high current density level of 10 A g^{-1} through 6,000 charge-discharge cycles. For measuring frequency-dependent impedance behavior, an initial open-circuit state was attained for half an hour, after which a small sinusoidal perturbation of voltage (10 mV) was applied to the sample over a wide range of frequencies ranging from 100 kHz to 10 mHz.

2.4 Electrode Preparation

The working electrodes were fabricated by blending active material (pristine NiFe-LDH or NiFe-LDH/graphene), carbon black (conductive additive), and PVDF binder in the ratio of 85:10:5. The mixture was dispersed in NMP and combined with a mortar and pestle for 30 minutes to produce thick slurry. The carbon paper of dimensions 1 cm × 2 cm was coated with the slurry. The mass loading of the active material was approximately 2 mg. Coated electrodes were vacuum-dried at 80 °C for 12 hours to thoroughly eliminate any remaining NMP before electrochemical testing. The electrode fabrication method is summarized in Figure 2.

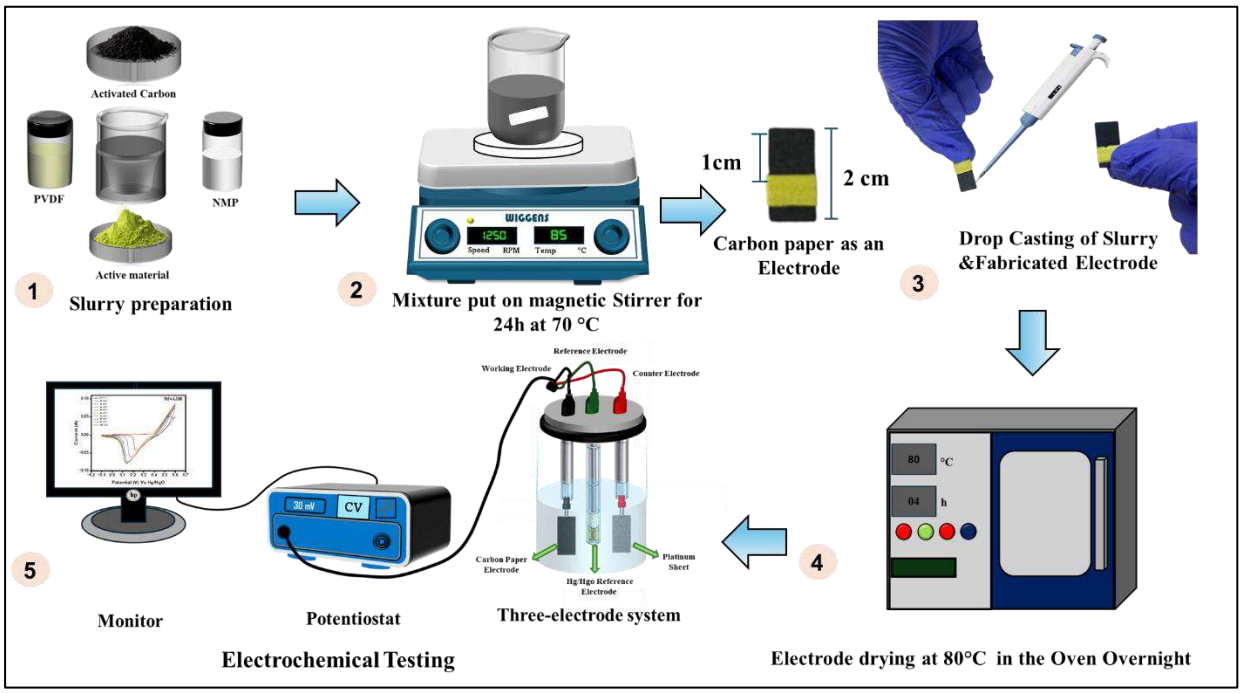


Figure 2. Schematic depicting the step-by-step process of slurry to electrode fabrication.

3. Results & Discussion

3.1 Physical Characterization

3.1.1 XRD Analysis

X-ray diffraction (XRD) investigation was conducted to examine the phase formation, crystallographic purity, and structural properties of the synthesized materials [29]. The XRD patterns of bare NiFe-LDH and NiFe-LDH@Graphene are depicted in Figure 3(a). The diffraction peaks found at 2θ values ~ 11.3°, 22.6°, 34.4°, 38.7°, 45.8°, 59.9°, and 61.0° were attributed to the diffraction from crystallographic planes (003), (006), (012), (015), (018), (110), and (113), respectively. These planes are typical of rhombohedral NiFe-LDH with space group R-3m, matching the reference pattern JCPDS Card No. 98-005-2835 [30-31]. The intense basal reflection corresponding to the (003) plane near 11° confirms the ordered stacking of brucite-like hydroxide layers along the crystallographic c-axis, while the prominent (110) reflection validates the in-plane hexagonal arrangement of Ni^{2+} and Fe^{3+} cations within the hydroxide sheets [32,33]. The XRD patterns demonstrate that the NiFe-LDH@Graphene composite exhibited all characteristic diffraction peaks of pristine NiFe-LDH, with no emergence of impurity peaks, signifying that the integration of graphene did not modify the crystal structure or cause any phase transformation during the hydrothermal synthesis process. The absence or weak intensity of the characteristic graphene diffraction peak may be attributed to its low content and high exfoliation within the composite matrix [33-35].

The mean crystallite sizes were calculated based on the Debye-Scherrer formula using the half-width at half maximum of the most intense (003) Bragg diffraction peak for all synthesized compositions:

$$D = \frac{K\lambda}{\beta\cos\theta} \quad [1]$$

The pure NiFe-LDH formed well-resolved diffraction peaks having a crystallite size of 7.6 nm, while the NiFe-LDH@Graphene nanocomposite resulted in broad diffraction peaks and a crystallite size of 6.7 nm. Larger crystallite size for pristine NiFe-LDH relative to NiFe-LDH@Graphene is linked to their distinct nucleation and growth processes involved in the synthesis method. For pristine NiFe-LDH, crystal growth is unrestricted since there are no physical barriers, and thus continuous stacking and growth of brucite-like hydroxide layers take place. This explains why pristine NiFe-LDH has a larger crystallite size and well-defined diffraction peaks, implying higher crystalline domains. Graphene serves as a 2D conductive as

well as nucleation and growth surface for LDHs [36]. This material has a large specific surface area and numerous defects/sites to facilitate quick anchoring and thus fast nucleation of Ni^{2+} and Fe^{3+}ions. Graphene, however, imposes physical restrictions on crystal growth while inhibiting agglomeration and stacking of LDH nanosheets.

3.1.2 Fourier-transform Infrared Spectroscopic Analysis

The vibrational energy spectrum characterized using FTIR spectroscopy offers clear insights into the molecular structure environment of pristine NiFe-LDH and NiFe-LDH@Graphene composite, as shown in Figure 3b. Various phonon modes that are highly indicative of the presence of hydrotalcite layered double hydroxide structures can be distinctly identified from the spectrum of the unmodified NiFe-LDH material [31,32]. The pronounced and broad high-intensity absorption band located at 3397 cm^{-1} represents the overlapped phonon modes arising from the O-H stretch vibrations occurring in two different molecular environments, namely the hydroxyl groups bonded to the metal centers in the octahedral coordination arrangement in the cationic layers in the brucite structure and the hydrogen-bonded water molecules in the interlayer nano space region. The sharp absorption peak at 1636 cm^{-1} results from the H-O-H scissoring vibration modes of the crystalline interlayer water molecules [33,34].

The absorption band ranging between 1356 and 1122 cm^{-1} corresponds to the asymmetric and symmetric stretching vibrations of the NO_3^- anions and is present within the positive interlayer gallery region as compensating charges due to the presence of the precursor nickel nitrate [33]. The low-energy vibration occurring at 645 cm^{-1} is assigned to metal-oxygen vibrations involving stretching of Ni-O and Fe-O bonds within the MO_6 edge-sharing complexes. This vibration depends upon the reduced mass of the metal-oxygen oscillator, along with the bond force constant.

Examining the composite spectral profile of NiFe-LDH@Graphene, all intrinsic phonon vibration modes associated with the parent metal hydroxide compound are retained completely without the slightest wavenumber shifting or alteration of relative intensity, indicating unambiguously that the inclusion of graphene into the composite does not induce any electronic disturbance to the local force constants of the M-O and O-H bonds, which vibrate in the brucite layer [34]. The lack of perturbation of intrinsic phonon modes of the LDH phase proves that the role of graphene is to function solely as a conductive phase and not a modifying one to the intrinsic hydroxide structure. In addition, the observation of a weak absorption band arising

from the C=C stretching vibrations of the sp^2 hybridized graphene phase indicates the successful inclusion of graphene within the composite.

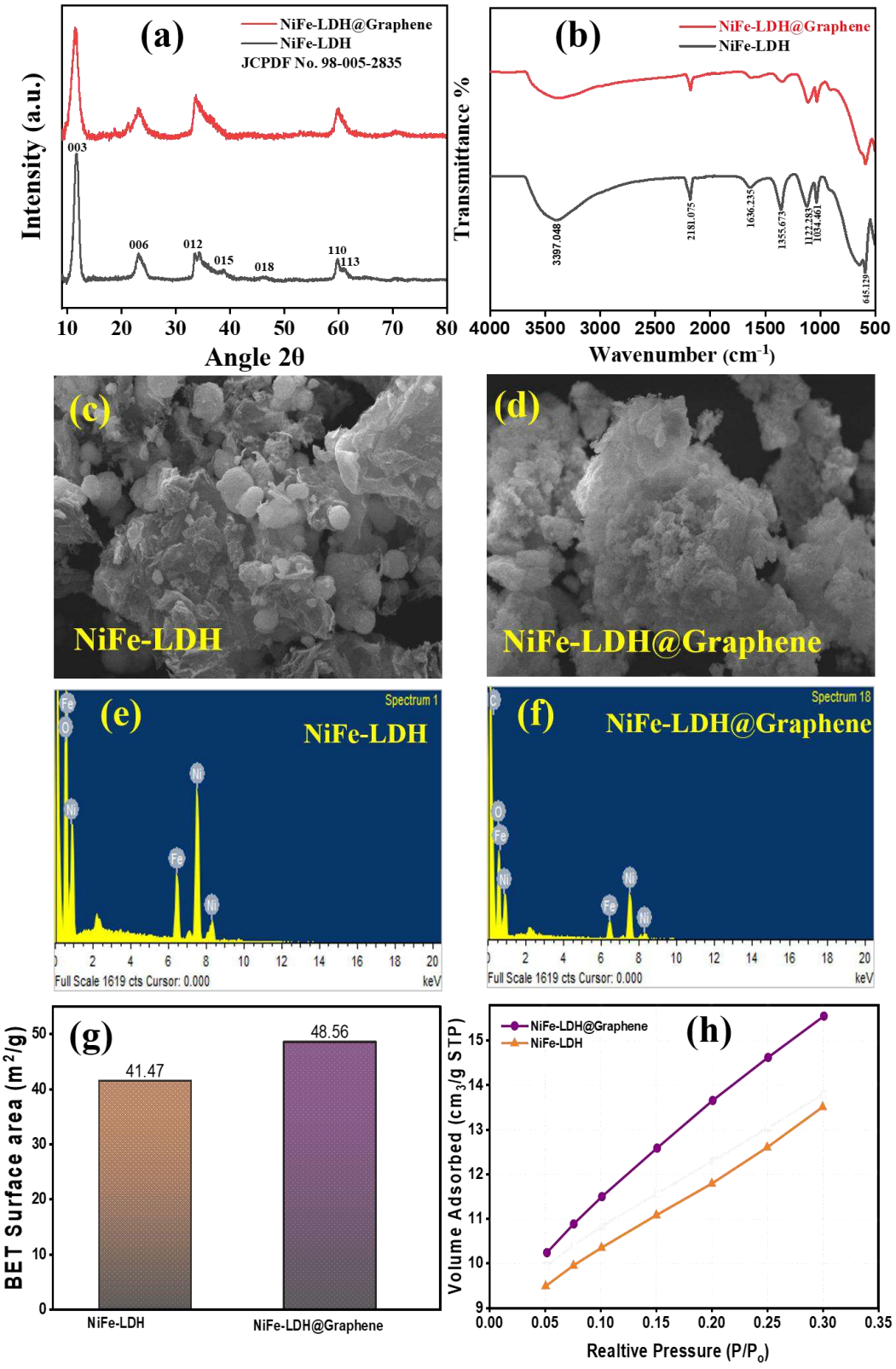


Figure 3. (a) X-ray diffraction patterns; (b) FTIR spectra; (c-d) FESEM images; (e-f) elemental mapping of Ni, Fe, O, and C elements in EDS; and (g-h) BET analysis of NiFe-LDH and NiFe-LDH@Graphene samples.

3.1.3 Morphological Analysis

Surface topology and microstructural organization of the fabricated NiFe-LDH and NiFe-LDH@Graphene compositions were systematically probed through field-emission scanning electron microscopy, with representative micrographic evidence presented in Figure 3(c-d). From Figure 3(c), the pristine NiFe-LDH shows a characteristic layered structure consisting of ultrathin, curved, and interwoven nanosheets [37]. These nanosheets have formed a loosely aggregated three-dimensional network-like structure owing to their densely intertwined nature, thereby creating a large surface area with numerous electrochemically active sites [38]. The NiFe-LDH@Graphene hybrid material illustrated in Figure 3(d) had an interconnected sheet-like morphology wherein the NiFe-LDH nanosheets were evenly formed and dispersed onto the surface of the wrinkled graphene sheets. Due to their two-dimensional form, graphene and LDH sheets facilitate the formation of interfaces that allow good integration of the layers. Such tight coupling makes it possible to enable electron transfer via the graphene networks while simultaneously increasing ion mobility within the entire composite. In addition, the graphene sheets helped avoid agglomeration and stacking of the LDH nanosheets. Elemental mapping and energy dispersive X-ray spectroscopy analysis of the NiFe-LDH@Graphene composite (Fig.3 e-f) revealed an excellent homogeneity of Ni, Fe, O, and C elements throughout the whole composition. The excellent distribution of the Ni, Fe, and O peaks indicated the successful crystallization of the NiFe-LDH phase, whereas the excellent distribution of the C peaks clearly demonstrated the successful incorporation of graphene within the layered structure of hydroxides. In addition, no elemental segregation at all clearly indicates the intimate interaction between the nanosheets of NiFe-LDH and the graphene matrix.

3.1.4 Internal Structure and Composition Analysis

Morphological and crystallographic characterizations of the NiFe-LDH@Graphene heterostructural composite were systematically accomplished through high-resolution transmission electron microscopy, with a representative micrograph presented in Figure 4. The low-magnification TEM images (Figure 4a-e) demonstrated ultrathin NiFe-LDH nanosheets homogeneously anchored on the transparent graphene sheets, thus confirming the formation of a well-integrated layered heterostructure, as suggested by FESEM micrographs. The HRTEM micrograph (Figure 4g-h) confirmed the presence of sharp lattice fringes with a separation distance of 0.387 nm between two adjacent planes, which matched the crystallographic plane (006) of rhombohedral NiFe-LDH [39-41]. The interplanar distance value obtained from HRTEM was quite similar to that determined by XRD. In addition, the SAED patterns (Figure

4f) showed concentric rings, which are typical of polycrystalline materials. The diffraction rings identified corresponded to the crystallographic planes (003), (006), (012), and (110) of NiFe-LDH. The appearance of diffraction rings rather than diffraction spots signifies the presence of a nanocrystalline structure due to the random orientation of the crystal planes, in support of a small crystallite size determined from the XRD technique.

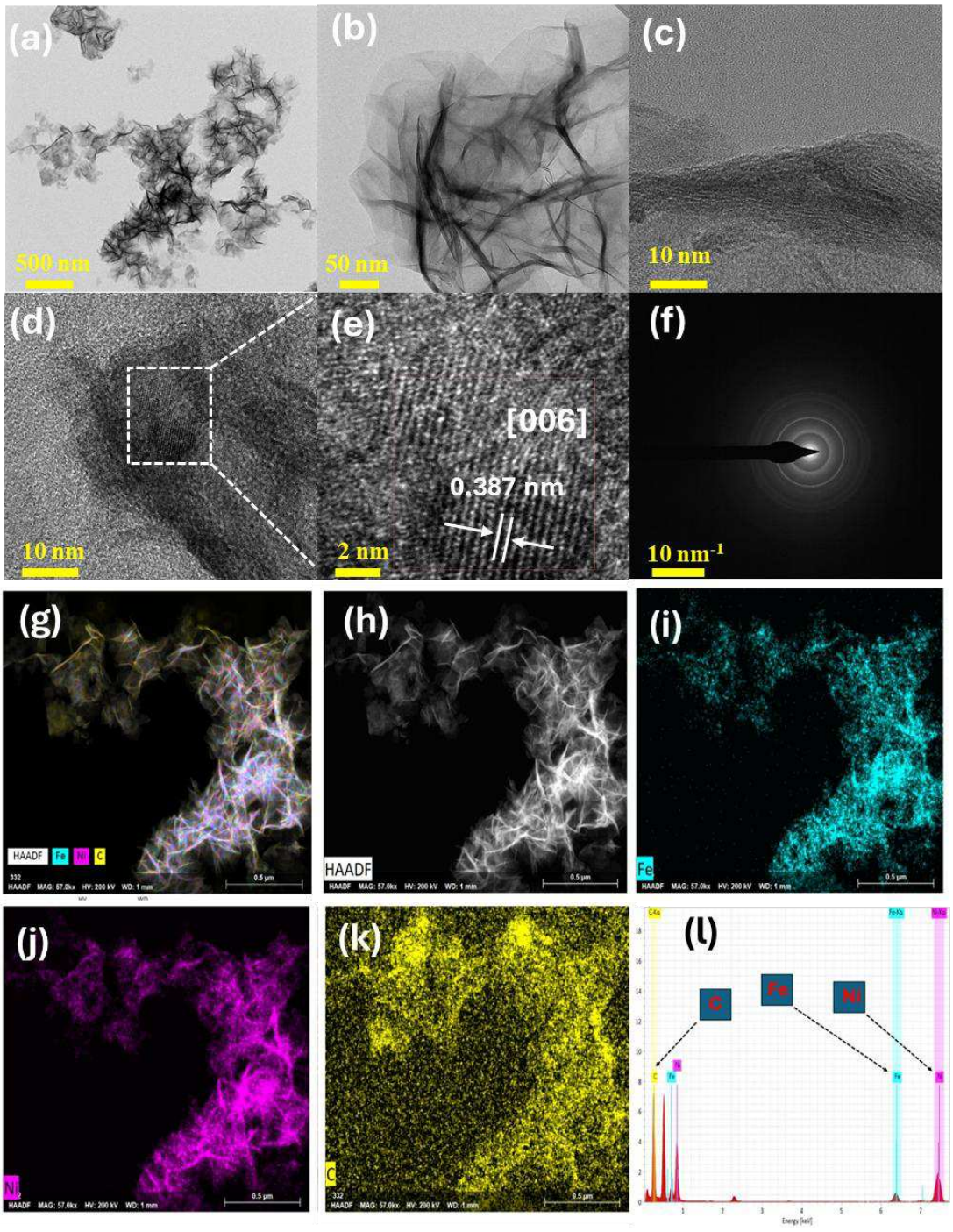


Figure 4. HRTEM analysis of the synthesized NiFe-LDH@Graphene material: (a-c) HRTEM images at various magnifications displaying the ultrathin, wrinkled, and sheet-like layered morphology; (d,e) enlarged HRTEM

images displaying clear lattice fringes with an interlayer spacing of 0.387 nm; (f) HAADF-STEM elemental mapping analysis of the composite material: (g,h) HAADF-STEM images, (i) Fe elemental mapping, (j) Ni elemental mapping, (k) C elemental mapping, and (l) Corresponding EDS spectrum confirming the distribution of Fe, Ni, and C elements within the composite structure.

The chemical composition and homogeneity of the NiFe-LDH@Graphene composite were examined by elemental mapping and energy-dispersive X-ray spectroscopy (EDS) studies, as shown in Figure 4. From HAADF-STEM images in Figures 4 (g and h), the NiFe-LDH nanosheets exhibit a sheet morphology and are uniformly distributed over the graphene substrate. Moreover, the elemental maps clearly demonstrate the uniform distribution of Fe, Ni, and C elements throughout the composite material, which proves that the formation of NiFe-LDH nanosheets on the surface of graphene was successful. While the distribution of element C indicates the inclusion of graphene in the composite material, the uniform distribution of Ni and Fe also indicates the successful development of the LDH phase. Moreover, the EDS spectrum depicted in Figure 4(l) clearly illustrates the presence of Ni, Fe, O, and C elements without any trace of impurities in the synthesized NiFe-LDH@Graphene composite material. This signifies that the fabricated composite material is of very high purity.

3.1.5 BET Surface Area Analysis

Quantitative textural analysis, including measurement of specific surface area and assessment of mesoporous structure for NiFe-LDH and NiFe-LDH@Graphene electrodes, was conducted by means of low-temperature nitrogen physisorption isotherm analysis with respective adsorption isotherms shown in Figure 3(g-h). The overlapping adsorption curves before the hysteresis region indicate monolayer-multilayer adsorption behaviour on the surfaces of the materials. Applying the Brunauer-Emmett-Teller (BET) method, the exact surface area of Pristine NiFe-LDH was determined to be 41.47 $m^2 g^{-1}$, which is typical for hydrothermally produced LDH materials where partial nanosheet restacking limits accessible surface area [42]. In comparison, the NiFe-LDH@Graphene composite has a much higher BET surface area of 48.56 $m^2 g^{-1}$, representing a 17.1% increase over pure NiFe-LDH. The increased surface area is due to the integration of graphene sheets, which effectively inhibit the agglomeration and restructuring of LDH nanosheets, exposing more electrochemically accessible active sites and permitting accelerated ion transport inside the mesoporous framework.

3.2 Electrochemical Characterization

3.2.1 Cyclic Voltammetry

A three-electrode cell containing 6 M KOH electrolyte was used for recording the electrochemical characteristics of pristine NiFe-LDH and NiFe-LDH/graphene electrodes through cyclic voltammetry (CV). These characteristics have provided simultaneous insight into redox mechanisms, ion transport dynamics, and the electrochemical consequences of graphene integration [43,44]. Electrochemical sweeping voltammetry was carried out over the range of -0.4 to +0.4 V relative to Hg/HgO with scan rates ranging from 10 to 100 mV/s, with characteristic voltammograms depicted in Figure 5(a,b). Both electrodes display strong anodic and cathodic current peaks throughout the range of scan rates observed, which indicates the presence of battery-type Pseudocapacitance due to diffusion-controlled Faradaic redox reactions rather than surface capacitance. This is because these peaks result from the redox reactions that take place between Ni^{2+}/Ni^{3+} and Fe^{2+}/Fe^{3+} ions of the brucite-like hydroxide structure under an alkaline environment, where the nonlinear and asymmetrical behavior of the charge/discharge curve confirms the battery-type charging nature:

$$Ni(OH)_2 + OH^- \rightleftharpoons \mathrm{NiOOH} + H_2O + e^- \quad [2]$$

$$Fe(OH)_2 + OH^- \rightleftharpoons \mathrm{FeOOH} + H_2O + e^- \quad [3]$$

Increasing the scan rate from 10 to 100 mVs^{-1} results in a systematic increase of the peak currents in both electrodes, as expected for the enhanced electrochemical activity at increased sweep speeds [42]. Alongside the trends, the anodic peak shifts towards higher potentials while the cathodic peak shifts towards lower potentials. This is due to the increasing electrode polarization effect, as well as due to the decreasing time scale of the OH^- ions' diffusion compared to the imposed sweep time. It is especially important to note that the potential gap formation occurs at a significantly slower pace in the case of NiFe-LDH/graphene, directly indicating the accelerated charge transfer kinetics associated with graphene inclusion in the composite structure. Indeed, the voltammogram obtained from NiFe-LDH/graphene exceeds the voltammogram obtained from pure NiFe-LDH at all scan rates considered (Figure 5 a,b). Comparison of the voltammograms recorded at 50 mVs^{-1} (Figure 5c) shows higher peak currents and higher integral areas, illustrating better accessibility of electroactive sites and lowered interfacial charge-transfer resistance.

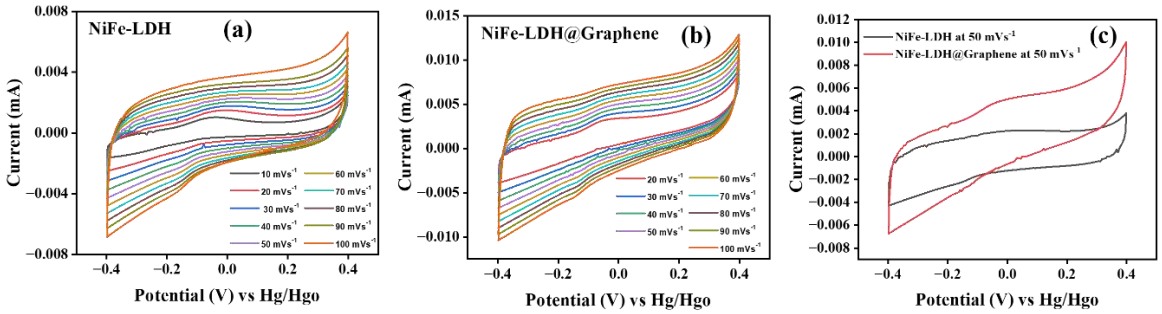


Figure 5. (a,b) NiFe-LDH and NiFe-LDH@Graphene CV curves obtained at various scan rates within the 10-100 mVs^{-1} range. (c) Cyclic voltammetry parameters of all three samples at 50 mVs^{-1} are compared.

3.2.2 Galvanostatic Charge-Discharge Characteristics

The electrochemical performances of the pristine NiFe-LDH and NiFe-LDH@Graphene electrodes were comprehensively studied via galvanostatic charge-discharge (GCD) experiments under various current densities of 1 to 5 A g^{-1} as presented in Figures 6(a-b). These two electrode samples showed a nonlinear charge-discharge profile with clear voltage plateaus while charging and discharging, suggesting that Faradaic charge transfer is more dominant in their charge storage mechanism compared to an ideal EDLC process. This finding supports the nature of batteries as demonstrated by the redox peaks in the CV experiments [45]. The calculated values for the specific capacitance were determined from the discharge curve by using Equation:

$$C_s = \frac{I \times \Delta t}{m \times \Delta V} \qquad [4]$$

and the results are presented in Table 1. The bare NiFe-LDH electrode showed a specific capacitance of 400 F g^{-1} at a current density of 1 A g^{-1}, and there was a steady decline in the specific capacitance value to 103.35, 53.96, 27.61, and 12.41 F g^{-1} at 2 to 5 A g^{-1} current densities, respectively. This could be explained by the inherent low electrical conductivity of the NiFe-LDH material. The NiFe-LDH@Graphene showed improved electrochemical behavior by presenting an impressive specific capacitance of 953 F g^{-1} when measured at 1 A g^{-1}. At elevated current densities of 2 to 5 A g^{-1}, the capacitances were still significant with values of 415.95, 242.68, 146.93, and 77.51 F g^{-1}, respectively. As illustrated in Figure 6c, the NiFe-LDH@Graphene showed much longer discharge times than pristine NiFe-LDH, suggesting better charge storage ability. The impressive enhancement in the capacitance is due to the highly conductive graphene structure that allows faster transportation of electrons, enhances charge transfer kinetics, prevents the aggregation of nanosheets, and increases the

availability of electrolytes to electroactive sites. The close interface interaction between graphene and NiFe-LDH nanosheets increases the effectiveness of the redox-active species and leads to improved electrochemical behavior and rate capability.

The graphene electrode demonstrated much better rate capability, measured as capacitance retention at high current density, compared with the 1 A g^{-1} performance (Figure 6c). At 5 A g^{-1}, the graphene composite remained 8.2% of the initial capacitance compared to 3.0% for pristine NiFe-LDH (Figure 6a). This substantial difference reflects improved ion diffusion kinetics and reduced polarization in hybrid materials. IR drop quantified as an instantaneous voltage decrease at discharge onset (visible in Figure 6a-c) followed by an inverse trend: pristine (180 mV) > graphene (62 mV) at 5 A g^{-1}, directly confirming that graphene scaffolds minimize ohmic and charge transfer resistances within composite electrodes. The minimal IR drop in the graphene composite (Figure 6c) validates excellent electronic connectivity established through intimate LDH-graphene interfaces observed in HRTEM.

The energy and power densities of the NiFe-LDH@Graphene electrode were calculated from the GCD data. A maximum energy density of 26.81 Wh kg^{-1} and a power density of 224.89 W kg^{-1} were achieved, confirming the excellent energy storage capability of the graphene-based composite electrode.

Table 1. Specific capacitances calculated at varying current densities for pristine and graphene-loaded NiFe-LDH samples.

S. No.	**Current Density (A g^{-1})**	**Pristine NiFe-LDH (F g^{-1})**	**NiFe-LDH@Graphene (F g^{-1})**
1	1	400	953
2	2	103	416
3	3	54	243
4	4	28	147
5	5	12	78

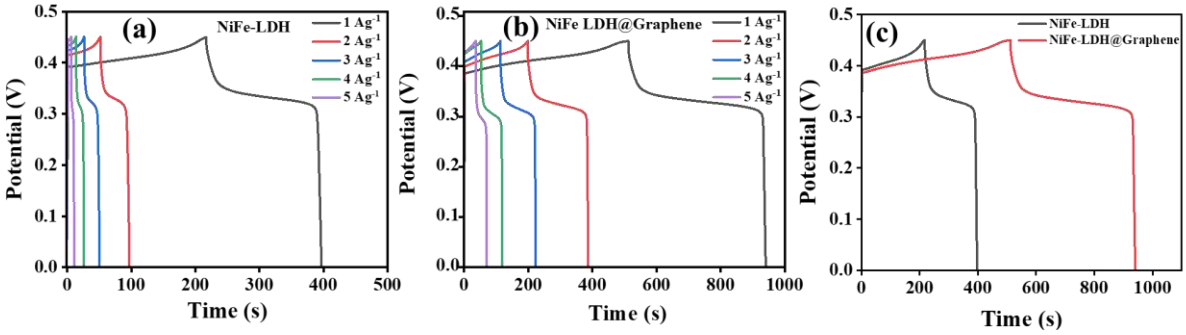


Figure 6. GCD characteristics for (a) NiFe-LDH, (b) NiFeLDH@graphene recorded at various current densities in the range (1-5 A g^{-1}), and (c) GCD plots at (1 A g^{-1}) for all three samples are presented for comparison purposes.

3.2.3 Power-Law Analysis of Charge Storage Kinetics

To assess the contributions of the diffusion-controlled process and the surface-controlled capacitive process in the total charge storage, a power-law equation was used as follows:

$$i = av^b \tag{5}$$

where *i* represent the peak current, *v* represents the scan rate, *a* is the proportionality constant, and *b* is the adjustable constant that helps understand the charge storage mechanism. A *b* value of 0.5 indicates that the electrochemical storage process is diffusion-controlled and dependent on ion diffusion within the electrodes. In contrast, *a b* value close to 1 indicates a surface-controlled capacitive process. Figure 7d displays the log(i_p) versus log(ν) plots derived from the anodic peak currents, in which the anodic peaks of the NiFe-LDH@Graphene composite were baseline-corrected to eliminate the residual non-faradaic background arising near the OER-onset region. Linear fittings of both datasets yielded highly correlated plots ($R^2 > 0.91$), enabling accurate extraction of the b-values [46,47]. The calculated b-values for the two electrodes are summarized in Table 2. The pristine NiFe-LDH exhibits a b-value of 0.419, which lies close to the theoretical diffusion-controlled limit of 0.5 and indicates that its charge-storage response is governed primarily by semi-infinite OH^- diffusion into the interlayer galleries during the Ni^{2+}/Ni^{3+} and Fe^{2+}/Fe^{3+} faradaic redox reactions. This near-diffusion-controlled behavior reflects the intrinsic conductivity limitation of the unsupported layered hydroxide framework and the sluggish transport of electrolyte ions to buried redox-active sites. In contrast, the NiFe-LDH@Graphene electrode exhibits a substantially higher b-value of 0.868, which approaches the surface-controlled limit of 1.0 and confirms the emergence of a dominant capacitive/surface-controlled contribution alongside the underlying faradaic process. This pronounced mechanistic shift (Δb = +0.45) is a direct consequence of the two-dimensional graphene network, which provides continuous and highly conductive pathways for rapid

electron transfer, exposes a greater density of surface-accessible Ni and Fe redox sites through face-to-face LDH-graphene contact, and shortens the effective OH^- diffusion length by suppressing LDH restacking. The elevated b-value therefore corroborates the superior specific capacitance and rate capability observed for the graphene-based composite in the CV and GCD measurements [46].

Table 2. Anodic b-values extracted from the power-law relation $i_p = av^b$ for NiFe-LDH and NiFe-LDH@Graphene electrodes.

S. No.	Sample	b-value	R^2
1	NiFe-LDH	0.419	0.910
2	NiFe-LDH@Graphene	0.868	0.994

3.2.4 Electrochemical Impedance Spectroscopy

Electrochemical impedance spectroscopic analysis was carried out to obtain quantitative insight into interfacial charge transfer and ionic transport mechanisms for both the developed electrode materials. Nyquist spectra of bare and NiF-LDH@Graphene electrodes are shown in Figure 7(a). In the high-frequency regime, the electrodes showed a usual semicircle, while in the low-frequency regime, they showed an almost straight-line portion [47-48]. The charge transfer resistance (R_{ct}) at the electrode-electrolyte interface is represented by the high-frequency semicircle, whereas ion diffusion in the electrodes is represented by the low-frequency straight line [45]. To obtain important electrochemical data from the experimental results, the obtained Nyquist plots were analyzed using a hypothetical circuit model that is made up of four elements, which consist of electrolyte resistance (R_s), charge transfer resistance at the interface (R_{ct}), constant phase element (CPE) for taking care of the non-ideality of capacitors, and Warburg impedance. Fitting results revealed a systematic reduction in resistances with carbon incorporation: pristine NiFe-LDH (R_s = 10.5 Ω, R_{ct} = 120 Ω) > NiFe-LDH@Graphene (R_s = 4.2 Ω, R_{ct} = 28 Ω). The NiFe-LDH@Graphene composite revealed a 77% decrease in the charge transfer resistance (Rct) in comparison to pure NiFe-LDH, thus validating the enhanced charge transfer kinetics due to the highly interactive nature of NiFe-LDH nanosheets and graphene. This significant resistance reduction highlights the capability of graphene in facilitating efficient electron transport through the continuous electron pathway and ensuring high conductivity in the electrode. Moreover, the decreased Rct signifies rapid electron transfer reaction and reduced electrode polarization, which improves the electrochemical performance of NiFe-LDH@Graphene. Steeper low-frequency slopes for the hybrid electrode indicated improved ion diffusion kinetics, consistent with b-value analysis. This combination of minimized charge transfer resistance and enhanced ion transport explains the superior rate capability and reduced IR drop observed in galvanostatic measurements.

3.2.5 Cycling Stability Performance

Electrochemical durability over a period of prolonged galvanostatic stressing is an inherent requirement of supercapacitor electrode materials that have practical utility [49]. Cycling stability of bare NiFe-LDH and NiFe-LDH@Graphene was systematically determined using 6,000 continuous cycles performed at a constant current density of 10 A g^{-1}, whereby the corresponding capacitance retention was obtained experimentally and shown in Figure 7c. Pristine NiFe-LDH showed degradation in its capacity with every cycle and lost about 27% of its capacity over 6,000 cycles. Restacking LDH nanosheets, volume change with redox

reactions, and loss of electrical connection between the active material and current collectors are the causes of electrode capacity loss [50]. In contrast to that, the performance of the NiFe-LDH@Graphene electrode proved to be much better, allowing it to keep 90.2% of its capacitance after 6,000 charge-discharge cycles (see Table 3 below), which is almost 23% higher than in the case of pristine NiFe-LDH. Additionally, the loss of capacitance for the graphene-modified electrode was 1.63% per 1,000 cycles, which is less than one-third of that of pristine NiFe-LDH (4.45% per 1,000 cycles). The above findings clearly suggest that graphene significantly enhances the cyclic stability of LDH electrodes. The durability of LDH-based composite electrodes is enhanced by graphene through a variety of synergistic mechanisms, including improving their electrochemical stability over time. As a robust 2D structure with high mechanical compliance, graphene exerts a moderating effect on the volumetric strain produced during multiple Faradaic cycles, distributes localized mechanical loads evenly across the electrode surface, and helps prevent structural failure modes (e.g., nanosheet cracking, interfacial delamination, and layer collapse). This has been demonstrated by Yao et al. [50], who showed that the incorporation of rGO into Co_3O_4 nanosheet arrays can relieve the lattice strain created by Faradaic cycling, which corresponds with improved long-term cycling performance for the composite. In addition to being a structurally supportive material, graphene also provides a second function within the composite structure; it acts as a 2D physical spacer that prevents LDH nanosheet restacking/aggregation and provides a continuous supply of electrochemically accessible surface sites and ion-transport pathways throughout prolonged operation. Li et al.[51] also confirm this mechanism through their work demonstrating that rGO support led to the successful creation of a CoAl-LDH/rGO sheet-on-sheet heterostructure, which reduced nanosheet aggregation, maintained many electrochemically active sites, and exhibited 92.9% capacitance retention over 8000 charge-discharge cycles due to the establishment of quick and reversible pathways for charge transport through the rGO matrix. In addition, strong electrostatic and covalent bonds between the graphene and layered double hydroxide (LDH) will anchor the active material to the conductive scaffold, therefore dramatically reducing the likelihood of the active phase dissolving or detaching from the conductive scaffold over time. The electrical conductivity of graphene and the percolating network of graphene will allow for faster transfer of electrons at the interface, lower internal resistance, and increased utilization of the redox-active center sites. All these results show that the integration of graphene into other structurally similar LDH materials has a very good mechanical basis and a very broad opportunity for engineers to increase both the

capacitance retention and the long-term electrochemical durability of LDH-based electrode materials.

Table 3. consolidates the capacitance retention characteristics and coulombic efficiency trends recorded across extended charge-discharge cycling at 10 A g^{-1} for each synthesized electrode material.

S. No.	Sample	Initial ($F\ g^{-1}$)	Final ($F\ g^{-1}$)	Retention (%)	Fade (%/1000 cycles)
1	NiFe-LDH	400	293	73.3	4.45
2	NiFe-LDH@Graphene	953	860	90.2	1.63

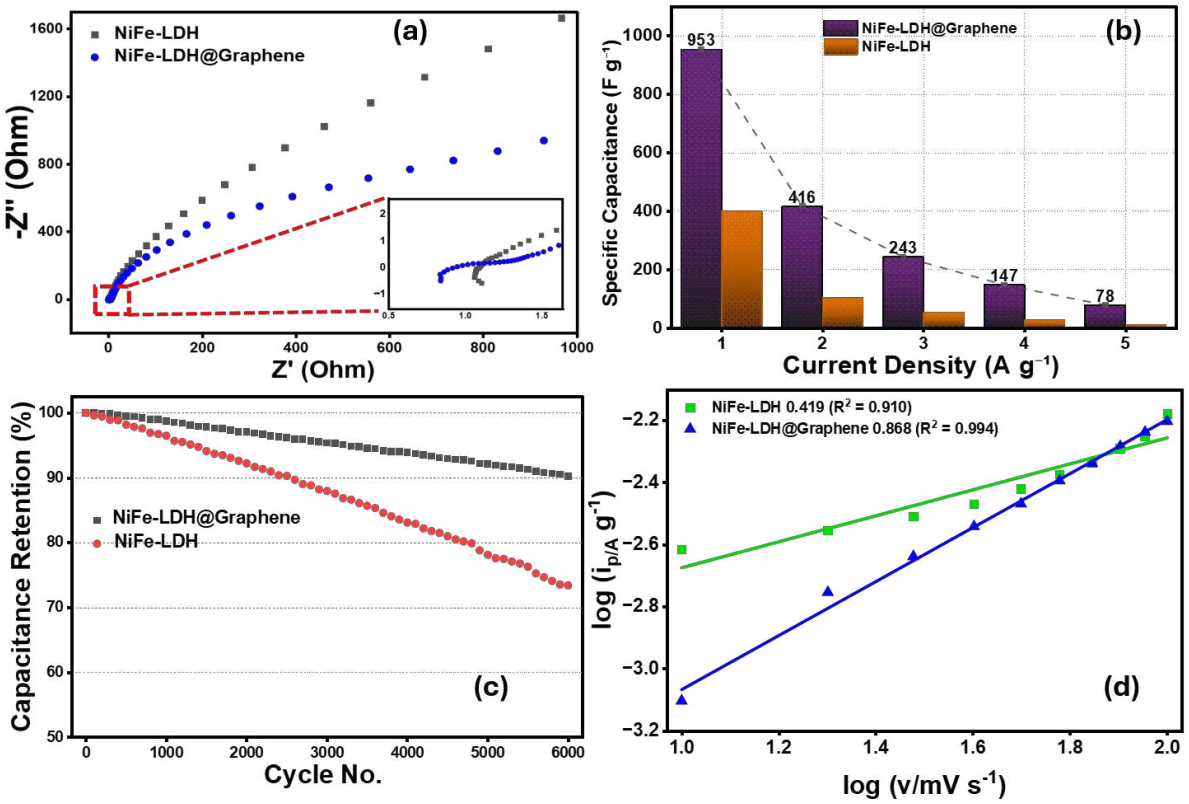


Figure 7. Electrochemical characterization of bare and graphene-coated NiFe-LDH electrodes: (a) EIS Nyquist plots showing charge-transfer and ion-diffusion behavior; (b) specific capacitance vs. current density relationship showing rate performance; (c) capacitance retention over 6,000 cycles of charging-discharging; and (d) determination of b value from the log(i)-log(ν) plot, which indicates the importance of surface-controlled vs. diffusion-controlled charge storage mechanisms.

3.2.6 Performance Benchmarking

To compare the electrochemical performance of the NiFe-LDH@Graphene electrode to that of other super-capacitive materials based on NiFe-LDH, a thorough investigation of the literature was conducted, and the results are shown in Table 4. The NiFe-LDH@Graphene electrode

prepared in this study exhibited a remarkable specific capacitance of 953 F g^{-1} when the current density was 1 A g^{-1}, which was about 2.4 times higher than that of pristine NiFe-LDH. Despite the numerous reports in the literature about higher capacitance values by employing material engineering techniques like elemental doping, growing directly on conductive substrates, or synthesizing hierarchical heterostructures, these approaches commonly require complicated fabrication processes, high synthesis costs, or multi-step processes. On the other hand, the already developed NiFe-LDH@Graphene hybrid provides significant electrochemical benefits via a simple in-situ growth approach that improves conductivity, electrochemical site availability, and charge transfer kinetics. The material retained 90.2% of its specific capacitance after 6,000 charge-discharge cycles at a current density of 10 A g^{-1}, indicating excellent stability. The high specific capacitance, outstanding rate capability, and high cycle stability clearly suggest that graphene incorporation into the structure was extremely successful in optimizing the electrochemical properties of NiFe-LDH. This study demonstrates that NiFe-LDH@Graphene is a promising contender for future supercapacitors.

Table 4. Comparative electrochemical performance of NiFe-LDH-based supercapacitor electrodes with literature-reported data. All specific capacitance values reported were estimated from GCD characteristics recorded at a current density of 1 A g^{-1}.

Electrode Material	**Synthesis Method**	**Electrolyte (KOH)**	**Configuration**	**Specific Capacitance (F g^{-1})**	**Cycling Stability**	**Test Cycles (A g^{-1})**	**Ref.**
NiFe-LDH@CNT	Hydrothermal	6 M	2-electrode (device)	1243.0	87.0%	6000 (10 A g^{-1})	[12]
GNS/NiAl-LDH	Hydrothermal	6M	3- electrode	781.5	–	200	[25]
NiFe-LDH/MXene	Hydrothermal	3M	3-electrode	720.2	86.0 %	1000 (10 A g^{-1})	[26]
$NiCo_2S_4$@NiFe-LDH	Hydrothermal	3M	3-electrode	827.0	90.2 %	12000 (5 A g^{-1})	[27]

3D Co-Al-LDH	Hydrothermal	2 M	3-electrode	838.0	95.0 %	20000 (5A g^{-1})	[28]
Ce-NiCo-LDH/CNT	Coprecipitation	1 M	3-electrode	187.2	85.6 %	9000	[29]
NiFe-LDH (spherical, 4:1)	Ultrasound-assisted	6 M	3-electrode	168.0	–	–	[30]
NCS@f-MWCNT	Hydrothermal	6M	2-electrode	186.0	82.0 %	5000 (10 A g^{-1})	[40]
NiCr-LDH/CNT	Hydrothermal	6 M	2-electrode	891	86.4 %	5000 (10 A g^{-1})	[44]
Ni_3Fe_1-LDH nanosheets	Green chemical synthesis	6 M	3-electrode	1923	81.4%	5000 (10 A g^{-1})	[45]
NiFe-LDH/rGO/Ni foam	Two-step electrodeposition	3 M	3-electrode	1462.5	64.7%	2000 (5 A g^{-1})	[46]
NiFe-LDH/RGO/CNF	One-step hydrothermal	6 M	2-electrode (device)	1330.2	64%	5000 (5 A g^{-1})	[47]
NiFe-LDH (pristine)	**Hydrothermal**	**6 M**	**3-electrode**	**400**	**73.3%**	**6000 (10 A g^{-1})**	**This work**
NiFe-LDH@Graphene	**Hydrothermal**	**6 M**	**3-electrode**	**953**	**90.2%**	**6000 (10 A g^{-1})**	**This work**

4. CONCLUSIONS

NiFe-LDH@Graphene composite with a highly porous nanostructure has been synthesized through a straightforward one-step hydrothermal process. The successful preparation of the nanocomposite and the retention of the LDH structure have been characterized by XRD, FTIR, FESEM, TEM, and elemental mapping studies. The results indicate that, from the structural analysis, graphene played the role of a good conducting material for the deposition of NiFe-LDH nanostructured sheets. Moreover, mesoporosity of the prepared nanomaterials has been confirmed by nitrogen adsorption-desorption measurements. NiFe-LDH@Graphene nanostructured composite has a larger surface area (48.56 m^2 g^{-1}) compared to pristine NiFe-LDH (41.47 m^2 g^{-1}). Electrochemical studies revealed that the introduction of graphene greatly enhanced the ability of NiFe-LDH to store charge. The electrode made from NiFe-LDH@Graphene had an impressive specific capacitance of 953 F g^{-1} at a current density of 1 A g^{-1}, almost 2.4 times as high as that of pure NiFe-LDH (400 F g^{-1}). Furthermore, the NiFe-LDH@Graphene-based electrode showed better rate capability by maintaining a capacitance of 953, 415.95, 242.68, 146.93, and 77.51 F g^{-1} at currents of 1 to 5 A g^{-1}, respectively. This was due to the conductivity of the graphene network, which enhanced electron transportation and electrolyte access. The Electrochemical Impedance Spectroscopic measurements confirmed the decreased value of the charge-transfer resistance from 120 Ω to 28 Ω for the pristine and NiFe-LDH@Graphene compounds, respectively, proving faster kinetics of the charge transfer and improved electrical conductivity. Power Law Kinetics analysis confirmed the increased b-value from 0.419 to 0.868 with the introduction of graphene into the NiFe-LDH compound. Results from long-term cycling revealed the remarkable stability of the graphene-hybridized electrode. The NiFe-LDH@Graphene exhibited 90.2% capacitance retention even after 6,000 charge-discharge cycles conducted at 10 A g^{-1}, while pristine NiFe-LDH only had 73.3% capacitance retention under the same condition. Clearly, the superior resistance to capacity decay was attributable to the effect of graphene in preserving the nano-sheet structure. In conclusion, these results show that graphene is a good electrical conductor and can be used to enhance NiFe-LDH's electrochemical performance. The NiFe-LDH@Graphene nanocomposite's high specific capacitance, enhanced charge transfer mechanisms, strong rate performance, and remarkable cycling stability make it a potential electrode material for upcoming supercapacitor technologies. Future research could include studying the effects of graphene concentration, scaling up fabrication methods, as well as developing energy storage devices using the material.

ACKNOWLEDGMENTS

The Centre for Advanced Studies of AKTU Lucknow and the Central Instrumentation Laboratory of IIT Jodhpur are hereby sincerely thanked for their invaluable help provided during the experiment through their state-of-the-art facilities and equipment.

DATA AVAILABILITY STATEMENT

All datasets generated during this study are retained by the corresponding author and are available upon reasonable request.

AUTHORS CONTRIBUTION

Ruhi Siddiqui: Inaugural draft preparation, Visual data interpretation, Result authentication, Experimental execution, Experimental data management. **Moin Ali Siddiqui:** writing, review, and editing. **Chandresh Kumar Rastogi**: Writing-review & editing, Validation, Supervision, Data curation, Conceptualization. **Prashant Kumar Gupta**: Writing-review & editing, Visualization, Validation. **A.V Ullas**: Writing-review draft. **C. Manjunatha**: Data curation, Formal analysis.

CONFLICTS OF INTEREST:

All authors who contributed to this paper declare that no conflict of financial interest.

References

[1]. Aman, M., Konduparty, P., Sharma, S., Srivastava, R. P., Bhattacharyya, S., Sharma, V., Panwar, S., Gautam, P., & Omar, S. (2025). Layered double hydroxide-based composites for energy storage applications: Insights into supercapacitors and batteries. Journal of Energy Storage, 116, 116093. https://doi.org/10.1016/j.est.2025.116093

[2]. Sadavar, S. P., Mulik, S. V., Koyale, P. A., Sadavar, S. V., & Delekar, S. D. (2025). Advances in anion-intercalated layered double hydroxides for supercapacitors: study of chemical modifications and classifications. Materials Horizons, 12, 5031-5052. 10.1039/D4MH01860E

[3]. Shwetha, K. P., Kamath, M. S., Athreya, Y. N., Rastogi, C. K., Nagaraju, K., Khosla, A., & Manjunatha, C. (2024). Development of NiS@f-CNT nanocomposite-based high-performance supercapacitor coin cell prototype device. Journal of Energy Storage, 75, 109404. https://doi.org/10.1016/j.est.2023.109404

[4]. Zhang, L., Hu, X., Wang, Z., Sun, F., & Dorrell, D. G. (2018). A review of supercapacitor modeling, estimation, and applications: A control/management perspective. Renewable and Sustainable Energy Reviews, 81, 1868-1878. https://doi.org/10.1016/j.rser.2017.05.283

[5]. Zhang, Y., Hu, S., Li, C. E., Yan, X. H., Zhang, Y. Y., Yin, R. B., Zhang, R., Song, Y. Y., & Gao, H. L. (2025). Advanced strategies for enhancing the electrochemical performance of NiAl LDH electrodes in supercapacitors. Coordination Chemistry Reviews, 531, 216497. https://doi.org/10.1016/j.ccr.2025.216497

[6]. Varshney, G., Ranjan, P., & Sengupta, S. (2026). Enhanced anode performance in lithium-ion batteries enabled by graphite, MoS_2, and boron-based planar materials. Chemical Physics Letters, 870, 142737. https://doi.org/10.1016/j.cplett.2026.142737

[7]. Kaushik, P., Rastogi, C. K., Channegowda, M., Patel, A., & Gyanprakash, M. (2023). Investigating electrochemical properties of iron oxide-carbon nanotube composite for supercapacitor application. *Materials Today: Proceedings*, *74*, 324-328. 10.1016/j.matpr.2022.08.258

[8]. Yadav, N., Rastogi, C. K., Maurya, G., & Manjunatha, C. (2024). Fuel dependent combustion synthesis and electrochemical characteristics of nickel cobalt oxide nanoparticles. *Materials Today: Proceedings*, *111*, 37-43. 10.1016/j.matpr.2023.10.110

[9]. Yadav, D. K., Maurya, M. P., Raitani, K., Rastogi, C. K., Gyanprakash, M., Krishna, R. H., & Manjunatha, C. (2023). Effect of fuel concentration on supercapacitor cycling of Co3O4 fabricated via solution combustion method. *Materials Today: Proceedings*, *79*, 420-423. 10.1016/j.matpr.2022.12.267

[10]. Wang, Y., Chen, Z., Zhang, M., Liu, Y., Luo, H., & Yan, K. (2022). Green fabrication of nickel-iron layered double hydroxides nanosheets efficient for the enhanced capacitive performance. Green Energy & Environment, 7, 1053-1061. https://doi.org/10.1016/j.gee.2021.01.019

[11]. Lu, Y., Jiang, B., Fang, L., Ling, F., Wu, F., Hu, B., Meng, F., Niu, K., Lin, F., & Zheng, H. (2017). An investigation of ultrathin nickel-iron layered double hydroxide nanosheets grown on nickel foam for high-performance supercapacitor electrodes. Journal of Alloys and Compounds, 714, 63-70.https://doi.org/10.1016/j.jallcom.2017.04.197

[12]. Rao, A. C. V. M., Golla, S., Rastogi, C. K., & Channegowda, M. (2024). Enhanced electrochemical performance of NiFe-LDH@CNT nanocomposite for high-energy supercapacitors. ACS Applied Electronic Materials, 7, 48-63. https://doi.org/10.1021/acsaelm.4c01381

[13]. VM, A. C., Rastogi, C. K., Golla, S., Nagaraj, R., & Channegowda, M. (2026). Design and fabrication of efficient NiAl-LDH/CNT electrodes for high-performance supercapacitors with light-sensing functionality. Materials Science and Engineering: B, 325, 119069.10.1016/j.mseb.2025.119069

[14]. Li, Y., He, G., Huang, Z., HuangFu, H., Li, Z., Qiao, Y., & Shi, Z. (2024). High-performance NF-loaded F-NiFe-LDH/rGO nanoflower/nanosheet composite electrode material achieving enhanced specific capacitance and energy density for supercapacitor. Journal of Energy Storage, 101, 113954. https://doi.org/10.1016/j.est.2024.113954

[15]. Shwetha, K. P., Manjunatha, C., Kamath, M. S., Rastogi, C. K., Chaudhary, V., Maurya, G., Khosla, A., & Singh, R. (2023). Fabrication of super-high energy density asymmetric supercapacitor prototype device employing NiCo2S4@f-MWCNT nanocomposite. Journal of Energy Storage, 72, 108657. https://doi.org/10.1016/j.est.2023.108657

[16]. Wang, F., Wang, T., Sun, S., Xu, Y., Yu, R., & Li, H. (2018). One-step synthesis of nickel iron-layered double hydroxide/reduced graphene oxide/carbon nanofibres composite as electrode materials for asymmetric supercapacitor. Scientific Reports, 8, 8908. https://doi.org/10.1038/s41598-018-27171-0

[17]. Liu, H., Li, J., Wang, M., Liu, Y., Liu, J., & Cui, H. (2019). Controlled microstructure in two-dimensional Ni-Co LDH nanosheets-crosslinked network for high performance supercapacitors. Advanced Powder Technology, 30, 1239-1246.https://doi.org/10.1016/j.apt.2019.04.001

[18]. Altalhi, A. A., Mohamed, E. A., & Negm, N. A. (2024). Recent advances inlayered double hydroxide (LDH)-based materials: Fabrication, modification strategies, characterization, promising environmental catalytic applications, and prospective aspects. Energy Advances, 3, 2136-2151.10.1039/D4YA00272E

[19]. Duddi, R., Dhiman, S., Singh, A. K., Kamboj, N., & Kumar, S. (2025). Superior cycle stability and enhanced pseudocapacitive performance of NiAl-LDH decorated carbon cloth for supercapacitor application. Applied Surface Science, 679, 161298. https://doi.org/10.1016/j.apsusc.2024.161298

[20]. Xiao, Q., Yuan, Y., Zhu, J., Shi, Z., Li, Z., & Zhu, J. (2022). Carbonate doped nickel-cobalt layered double hydroxide for high performance asymmetric supercapacitors. Journal of Alloys and Compounds, 916, 165391. https://doi.org/10.1016/j.jallcom.2022.165391

[21]. Zhang, W., Zhu, Z., Zhu, L., Xu, X., Chen, X., Wang, X., & Lu, M. (2025). Defect-engineered heterostructured NiFe-LDH@CoNi-LDH nanocages via synergistic interface-oxygen vacancy modulation for high-energy-density supercapacitors. Chemical Engineering Journal, 500, 167235. 10.1016/j.cej.2025.167235

[22]. Li, R. Y., Shen, X. Y., Li, J., Zhao, D. P., Zhao, R. D., & Wu, F. F. (2025). Enhanced electrochemical performance of NiCo-layered double hydroxides: Optimal synthesis conditions and supercapacitor applications. Advanced Sustainable Systems, 9, 2400753. https://doi.org/10.1002/adsu.202400753

[23]. Kuang, H., Zhang, H., Liu, X., Chen, Y., Zhang, W., Chen, H., & Ling, Q. (2022). Microwave-assisted synthesis of NiCo-LDH/graphene nanoscrolls composite for supercapacitor. Carbon, 190, 57-67. 10.1016/j.carbon.2021.12.097

[24]. Pan, Y., Shen, J., Yang, L., Wang, Q., Hong, S., Dong, J., ... & Ang, E. H. (2026). In Situ Oxidation Suppresses Mn (III) Jahn–Teller Distortion in CoNi Layered Double

Hydroxides for Supercapacitors and Urea Electrooxidation. *Electrochimica Acta*, 149397.10.1016/j.electacta.2026.149397

[25]. Gao, Z., Wang, J., Li, Z., Yang, W., Wang, B., Hou, M., ... & Liu, L. (2011). Graphene nanosheet/Ni2+/Al3+ layered double-hydroxide composite as a novel electrode for a supercapacitor. Chemistry of Materials, 23(15), 3509-3516. https://doi.org/10.1021/cm200975x

[26]. Zhou, H., Wu, F., Fang, L., Hu, J., Luo, H., Guan, T., ... & Zhou, M. (2020). Layered NiFe-LDH/MXene nanocomposite electrode for high-performance supercapacitor. *International Journal of Hydrogen Energy*, *45*(23), 13080-13089. https://doi.org/10.1016/j.ijhydene.2020.03.001

[27]. Rabbani, S. S., Mustafa, H., Zafar, A., Javaid, S., Bakar, M. A., Nisar, A., ... & Ahmad, M. (2023). Nickel foam supported hierarchical NiCo2S4@ NiFe LDH heterostructures as highly efficient electrode for long cycling stability supercapacitor. *Electrochimica Acta*, *446*, 142098. 10.1016/j.electacta.2023.142098

[28]. Zai, J., Liu, Y., Li, X., Ma, Z. F., Qi, R., & Qian, X. (2017). 3D hierarchical Co–Al layered double hydroxides with long-term stabilities and high rate performances in supercapacitors. Nano-micro letters, 9(2), 21. https://doi.org/10.1007/s40820-016-0121-5

[29]. Dinari, M., Allami, H., & Momeni, M. M. (2020). Construction of Ce-doped NiCo-LDH@ CNT nanocomposite electrodes for high-performance supercapacitor application. *Energy & Fuels*, *35*(2), 1831-1841. https://doi.org/10.1021/acs.energyfuels.0c03764

[30]. Sanati, S., & Rezvani, Z. (2018). Ultrasound-assisted synthesis of NiFe-layered double hydroxides as efficient electrode materials in supercapacitors. Ultrasonics Sonochemistry, 48, 199-206.10.1016/j.ultsonch.2018.05.035

[31]. Siddiqui, M. A., Ahmed, S., Ansari, A., Choudhary, S. K., Negi, D. S., & Ranjan, P. (2025). Green synthesis of hematene for high-performance supercapacitor electrodes. Journal of Materials Science: Materials in Electronics, 36, 1304. https://doi.org/10.1007/s10854-025-15380-z

[32]. Wang, J., Polleux, J., Lim, J., & Dunn, B. (2007). Pseudocapacitive contributions to electrochemical energy storage in TiO_2 (anatase) nanoparticles. Journal of Physical Chemistry C, 111, 14925-14931. https://doi.org/10.1021/jp074464w

[33]. Shao, Y., El-Kady, M. F., Sun, J., Li, Y., Zhang, Q., Zhu, M., Wang, H., Dunn, B., & Kaner, R. B. (2018). Design and mechanisms of asymmetric supercapacitors. Chemical Reviews, 118, 9233-9280. https://doi.org/10.1021/acs.chemrev.8b00252

[34]. Saranraj, A., Abinaya, S., Lakshmi, U. S., Govindasamy, M., & Jose, S. P. (2025). Advancing supercapacitors with NiMn-LDH@V_2C MXene: A synergistic pathway to enhanced energy storage. Journal of Energy Storage, 129, 117284. https://doi.org/10.1016/j.est.2025.117284

[35]. Siddiqui, M. A., & Jaiswal, P. (2021). Photocatalytic behavior of ferroelectric materials: comparative study of $BaTiO_3$ and Ag-loaded $BaTiO_3$ for wastewater treatment. IOP Conference Series: Materials Science and Engineering, 1166, 012031. https://doi.org/10.1088/1757-899X/1166/1/012031

[36]. Powder Diffraction File, PDF-4+ 2024, International Centre for Diffraction Data (ICDD), Newtown Square, PA, USA.

[37]. Geim, A. K., & Novoselov, K. S. (2007). The rise of graphene. Nature Materials, 6, 183-191. https://doi.org/10.1038/nmat1849

[38]. Trasatti, S., & Petrii, O. A. (1992). Real surface area measurements in electrochemistry. Journal of Electroanalytical Chemistry, 327, 353-376. https://doi.org/10.1016/0022-0728(92)80162-W

[39]. Ahmed, S., Ansari, A., Bishwanathan, S., Siddiqui, M. A., Tailor, S., Gupta, P. K., Negi, D. S., & Ranjan, P. (2024). Electronic tongue based on ZnO/ITO@glass for electrochemical monitoring of spiciness levels. Langmuir, 40, 4434-4446.https://doi.org/10.1021/acs.langmuir.3c03763

[40]. Beena, S., Rastogi, C. K., Athreya, Y., Shwetha, K. P., Abraham, N., Viswanathan, S. B., Nagaraj, R., Kumar, K. N., Khosla, A., & Manjunatha, C. (2025). Unveiling the supercapattery behaviour of novel kotoite-type $Co_3(BO_3)_2$ nanoparticles. Journal of Energy Storage, 110, 115299. https://doi.org/10.1016/j.est.2025.115299

[41]. Tang, Y., Liang, Z., Jin, Y., Gao, S., & Zou, R. (2021). Understanding and tackling lattice manganese exfoliation and deactivation of battery-type NiMn-LDH in fast electrochemical energy storage. *Journal of Materials Chemistry A*, *9*(40), 23286-23295.DOI: 10.1039/D1TA06481A

[42]. Li, R. Y., Shen, X. Y., Li, J., Zhao, D. P., Zhao, R. D., & Wu, F. F. (2025). Enhanced Electrochemical Performance of NiCo-Layered Double Hydroxides: Optimal Synthesis Conditions and Supercapacitor Applications. *Advanced Sustainable Systems*, *9*(2), 2400753. https://doi.org/10.1002/adsu.202400753 .

[43]. Altalhi, A. A., Mohamed, E. A., & Negm, N. A. (2024). Recent advances in layered double hydroxide (LDH)-based materials: fabrication, modification strategies, characterization, promising environmental catalytic applications, and prospective aspects. *Energy Advances*, *3*(9), 2136-2151. https://doi.org/10.1039/D4YA00272E

[44]. Chavan, V. A., Shireesha, G., Rastogi, C. K., & Manjunatha, C. (2025). Nickel chromium-LDH/CNT composite for supercapacitors: Synergistic conductive network for superior energy storage. Journal of Power Sources, 654, 237807. https://doi.org/10.1016/j.jpowsour.2025.237807

[45]. Wang, Y., Chen, Z., Zhang, M., Liu, Y., Luo, H., & Yan, K. (2022). Green fabrication of nickel-iron layered double hydroxides nanosheets efficient for the enhanced capacitive performance. Green Energy & Environment, 7, 1053-1061. https://doi.org/10.1016/j.gee.2021.01.019

[46]. Li, M., Jijie, R., Barras, A., Roussel, P., Szunerits, S., & Boukherroub, R. (2019). NiFe layered double hydroxide electrodeposited on Ni foam coated with reduced graphene oxide for high-performance supercapacitors. Electrochimica Acta, 302, 1-9. https://doi.org/10.1016/j.electacta.2019.01.162

[47]. Li, Y., He, G., Huang, Z., HuangFu, H., Li, Z., Qiao, Y., & Shi, Z. (2024). High-performance NF-loaded F-NiFe-LDH/rGO nanoflower/nanosheet composite electrode material achieving enhanced specific capacitance and energy density for supercapacitor. Journal of Energy Storage, 101, 113954. https://doi.org/10.1016/j.est.2024.113954

[48]. Lu, Y., Jiang, B., Fang, L., Ling, F., Wu, F., Hu, B., Meng, F., Niu, K., Lin, F., & Zheng, H. (2017). An investigation of ultrathin nickel-iron layered double hydroxide nanosheets grown on nickel foam for high-performance supercapacitor electrodes. Journal of Alloys and Compounds, 714, 63-70.https://doi.org/10.1016/j.jallcom.2017.04.197

[49]. Ray, P. K., & Parida, K. (2025). Achievements, challenges, and stability of layer double hydroxide and carbon nanotube hybrid electrode materials for clean and sustainable energy storage supercapacitor application: an extensive review. *Materials Advances*, *6*(1), 84-116. https://doi.org/10.1039/D4MA00772G

[50]. Yao, T., Guo, X., Qin, S., Xia, F., Li, Q., Li, Y., ... & He, D. (2017). Effect of rGO coating on interconnected Co3O4 nanosheets and improved supercapacitive behavior of Co3O4/rGO/NF architecture. *Nano-micro letters*, *9*(4), 38. https://doi.org/10.1007/s40820-017-0141-9

[51]. Li, S., Cheng, P., Luo, J., Zhou, D., Xu, W., Li, J., ... & Yuan, D. (2017). High-performance flexible asymmetric supercapacitor based on CoAl-LDH and rGO electrodes. *Nano-Micro Letters*, *9*(3), 31 https://doi.org/10.1007/s40820-017-0134-8